J. Membrane Biol. 195, 109–120 (2003)
DOI: 10.1007/s00232-003-2049-1

The Journal of
Membrane
Biology

Transinhibition and Voltage-gating in a Fungal Nitrate Transporter

J. Boyd[1], **D. Gradmann**[2], **C.M. Boyd**[3]
[1]Institute for Marine Bioscience, National Research Council, Halifax, N.S., B3H 3Z1 Canada
[2]Abteilung Biophysik der Pflanze, Universität Göttingen, Untere Karspüle 2, 37073 Göttingen, Germany
[3]Department of Oceanography, Dalhousie University, Halifax, N.S., B3H 4J1 Canada

Received: 7 January 2003/Revised: 16 May 2003

Abstract. We have applied enzyme kinetic analysis to electrophysiological steady-state data of Zhou et al. (Zhou, J.J., Trueman, L.J., Boorer, K.J., Theodoulou, F.L., Forde, B.G., Miller, A.J. 2000. A high-affinity fungal nitrate carrier with two transport mechanisms. J. Biol. Chem. 275:39894–9) and to new current-voltage-time records from *Xenopus* oocytes with functionally expressed NrtA (crnA) $2H^+$-NO_3^- symporter from *Emericella* (*Aspergillus*) *nidulans*. Zhou et al. stressed two Michaelis-Menten (MM) mechanisms to mediate the observed nitrate-induced currents, $I_{NO_3^-}$. We show that a single straightforward reaction cycle describes the data well, pointing out that during exposure to external substrate, $S = (2H^+ + NO_3^-)_o$, the product concentration inside, $[P] = [H^+]_i^2 \cdot [NO_3^-]_i$, may rise substantially near the plasma membrane, violating the condition $[P] \ll [S]$ for MM kinetics. Here, $[P]$ and its changes during experimentation are treated explicitly. $K_{1/2} \approx 20$ μM for $I_{NO_3^-}$ at pH_o from Zhou et al. is confirmed. According to our analysis, NrtA operates between about 0.2 and 0.6 of the electrical distance in the membrane (outside 0, inside 1). In absence of thermodynamic gradients, the predominant orientation of the binding site(s) is probably inwards. The activity of the enzyme is sensitive to the transmembrane voltage, V, with an apparent gating charge of $+1.0 \pm 0.5$ for inactivation, and transition probabilities of 0.3–1.3 s^{-1} at $V = 0$. This gating mode impedes loss of cellular NO_3^- during depolarization.

Key words: *Emericella nidulans* — Kinetic *dIVt* analysis — NrtA — Triangular *V*-clamp — *Xenopus* oocytes

Correspondence to: D. Gradmann; email: dgradma@gwdg.de

Introduction

Experimental data have recently been reported on NO_3^--induced changes of current-voltage relationships, *dIV*, in *Xenopus* oocytes with functionally expressed NrtA (former crnA, Unkles et al., 1991; Glass et al., 2002) high-affinity nitrate transporter from *Emericella* (former *Aspergillus*) *nidulans* (Zhou et al. 2000). The dependence of these currents on the external NO_3^- concentration, $[NO_3^-]_o$, did not show simple Michaelis-Menten kinetics, MM, but went through a maximum around 100 μM $[NO_3^-]_o$. This behavior has been described by two MM, a normal, 'high-affinity' MM plus an inhibiting, 'low-affinity' MM (Zhou et al. 2000). A kinetic 6-state model was proposed to account for this behavior. This model was not treated numerically by corresponding fits. The MM analysis is based on the assumption of negligible $[NO_3^-]_i$, which has approximately been confirmed for whole oocytes but not for the particular space next to the interior side of the plasma membrane.

We have analyzed the data of Zhou et al. (2000) and have extended their study with further experiments. We present an ordinary 4-state model that provides a quantitative description of the experimental data in Fig. 4 of Zhou et al. (2000). To account for the apparent inhibition at high $[NO_3^-]_o$, we assume transinhibition by a local increase of $[NO_3^-]_i$ at the interior site of the symporter during the experimental procedure.

Zhou et al. (2000) presented and analyzed their experimental data as steady-state data without evidence for time-invariant behavior. We examined this point and found significant temporal changes of $[NO_3^-]$-induced currents, $I_{NO_3^-}$, with respect to temporal changes of $[NO_3^-]_o$. We also found relaxations in the temporal response of $I_{NO_3^-}$ upon changes of the

transmembrane voltage, V. These relaxations reflect the temporal behavior of the V-sensitive activity of the transporter. This behavior is well known for ion channels as 'V-gating'. Qualitatively, Blatt et al. have earlier (1997) noticed this V-sensitivity of a fungal nitrate transporter. For Na^+/glucose cotransporters (SGLT), Wright et al. (1994) have assigned relaxations upon V-changes to specific conformational changes within a 6-state reaction scheme. In the present study the enzymatic cycle and its V-sensitivity are treated as independent processes, because we lack information about coupling of these processes in NrtA.

Materials and Methods

Production of *Emericella nidulans* nrtA mRNA

The *E. nidulans* nitrate transporter gene, *nrtA*, formerly *crnA*, was kindly given to us by Dr. J. Kinghorn. It was supplied as cDNA with an N-terminal T7 fusion and a C-terminal His-tag in the vector pET21a (Novagen, Madison, WI). In order to make mRNA that would be stably expressed in *Xenopus* oocytes we subcloned the coding sequence of *nrtA* into the vector pSP64TS (Paul Wilson). pSP64TS carries *Xenopus* globin-flanking sequences on either side of a small polylinker, a polyA tail sequence and a phage SP6 promoter. The *nrtA* was amplified using PCR and the following primers: Enid up, 5′GGGTagatctGCCACC*ATG*GACTTCGCCAAGCTGCTGGTAGC3′ and Enid down, 5′CGGCtctaga*CT*-*A*CTCCCTCATCTGACTTTTCGGCAC3′. Lower-case letters indicate the *Bgl*II and *Xba*I sites, the consensus Kozak sequence is underlined, and the stop and start codons are italicized. The PCR fragment was cloned into the *Bgl*II and *Spe*I sites of vector pSP64TS to generate pSP64TS-Enid (complete sequence of this clone is available upon request).

MessengerRNA was made from pSP64TS-Enid linearized at the *Eco*RI site, using the mMessage mMachine kit from Ambion (Austin, TX). The mRNA was purified using NucAway Spin Columns also from Ambion and stored in water at −20°C until use; mRNA length and integrity were confirmed by formaldehyde agarose gel electrophoresis (*not shown*).

Preparation, Injection, and Electrophysiology of Oocytes

Oocytes were handled according to Goldin (1992). Briefly, oocytes were surgically removed from an adult female *Xenopus laevis* that had been anaesthetized for 20 minutes in a 0.2% solution of MS-222 (3-aminobenzoic acid ethyl ester; Sigma A 5040). They were routinely kept in ND96 medium (96 mM NaCl, 2 mM KC1, 1.6 mM $CaCl_2$, 1 mM $MgC1_2$, and 5 mM HEPES titrated to pH 6.5 with NaOH). For removal of their follicular membrane, the oocytes were treated for 1 hour with collagenase (2 mg Type 1A; Sigma C 9891) dissolved in 1 ml of Ca^{2+}-free OR2 medium (82.5 mM NaCl, 2 mM KC1, 1 mM $MgC1_2$, 1 mM Na_2HPO_4, 5 mM HEPES, pH 7.5 with NaOH). After the collagenase treatment the eggs were transferred again to ND96 medium.

Oocytes were injected with 50 nl of mRNA containing 1 μg mRNA/μl, using a Drummond Nanoject II injecting system. Injected oocytes were incubated in ND96 for three to five days on a rotary shaker at 18°C before use. Water-injected oocytes used as controls showed no significant inward currents induced by external nitrate.

Electrophysiological recordings of oocytes were made following two-electrode voltage-clamp techniques (Stühmer, 1992), using a Dagan TEV-200 voltage-clamp amplifier. Individual oocytes were placed in a slight depression in a trough 6 mm wide by 6 mm deep machined in a lucite block. A chosen test solution entered at one end of the trough flowed over the oocyte, and entered a chamber at the distal end of the trough where the solution was removed by aspiration. A manifold in the block allowed a single solution to be selected from six available solutions; any of the six could be selected by an electrical switch that controlled a bank of solenoid valves that controlled the flow from six reservoirs that fed the system by gravity. The front of a new solution reached the oocyte about two seconds after the solenoid valve was opened. External medium for experiments was ND96 with or without NO_3^-. The flow rate through the trough was about 0.5 ml · s^{-1}.

The protocol of voltage control used in the voltage-clamp procedure was a single, triangular wave that started at a specified holding voltage, V_h, then descended to the minimum, V_1, of the investigated V range (here −150 mV), then ascended to the maximum, V_2, of the V range (here +50 mV), and finally descended to V_h again, which was usually −40 mV. The V protocol was executed by steps of ±1 mV amplitude and 10 ms duration. Data were sampled synchronously (100 Hz) and low-pass filtered with a 20 Hz four-pole Bessel filter. Temporal changes of nonlinear current-voltage relationships (*IVt* records) could be recorded in 4 s with this protocol (for details *see* Gradmann and Boyd, 1999), thus avoiding drift artifacts more efficiently than with conventional, longer step protocols.

Theory

Figure 1 illustrates the model used here. Figure 1*A* shows an ordinary cyclic 4-state reaction scheme for a transporter. States 1 and 3 denote states that can react with internal substrates, and states 2 and 4 denote states exposed to external substrates. Apparent rate constants for binding reactions are $k_{31} = k^0_{31}[H^+]'^2_i[NO_3^-]'_i$ and $k_{42} = k^0_{42}[H^+]'^2_o[NO_3^-]'_o$, where the superscript ^{0} marks the fundamental rate constants when all substrate concentrations are specified at 1 mM, and c' the concentrations at the binding site of the enzyme. The binding reactions and debinding reactions (k_{13} and k_{24}) are not marked explicitly because they are assumed to be much faster than the translocation reactions, k_{12}, k_{21}, k_{34}, and k_{43}. They are represented, therefore, by equilibrium constants $K_1 = k_{31}/k_{13} = K^0_1[H^+]'^2_i[NO_3^-]'_i$ and $K_2 = k_{42}/k_{24} = K^0_2[H^+]'^2_o[NO_3^-]'_o$ for state 1 and state 2, respectively, where the superscript ^{0} denotes reference conditions again (all concentrations 1 mM).

In thermodynamic equilibrium under reference conditions (V = 0, and all substrate concentrations 1 mM, denoted by ^{0}), microscopic reversibility dictates: $k^0_{12}k^0_{43}K^0_1 = k^0_{21}k^0_{34}K^0_2$. Thus only five of the six parameters k^0_{12}, k^0_{21}, k^0_{34}, k^0_{43}, K^0_1, and K^0_2 are independent. We have arbitrarily chosen the first five of this series to be independent and $K^0_2 = K^0_1k^0_{12}k^0_{43}/k^0_{21}/k^0_{34}$.

It should be recalled that, in principle, ion transporters are enzymes with saturating turnover at large driving forces. In general, this results in sigmoid IV relationships, which can be used to determine seven independent system parameters when IV relationships are recorded at different substrate concentrations on both sides (Gradmann et al. 1987). With our assumption k_{12}, k_{21}, k_{34}, $k_{43} \ll k_{13}$, k_{31}, k_{24}, k_{42}, the 4-state reaction cycle has only five independent parameters. So, experimental steady-state IV recordings can be used to determine two additional system parameters, which are described next.

Compared to the theoretical non-linearities of the reaction cycle with one charge-carrying reaction step, many experimental results show weaker V-induced non-linearities. This finding is explained by partioning of the entire transmembrane voltage, V, amongst a se-

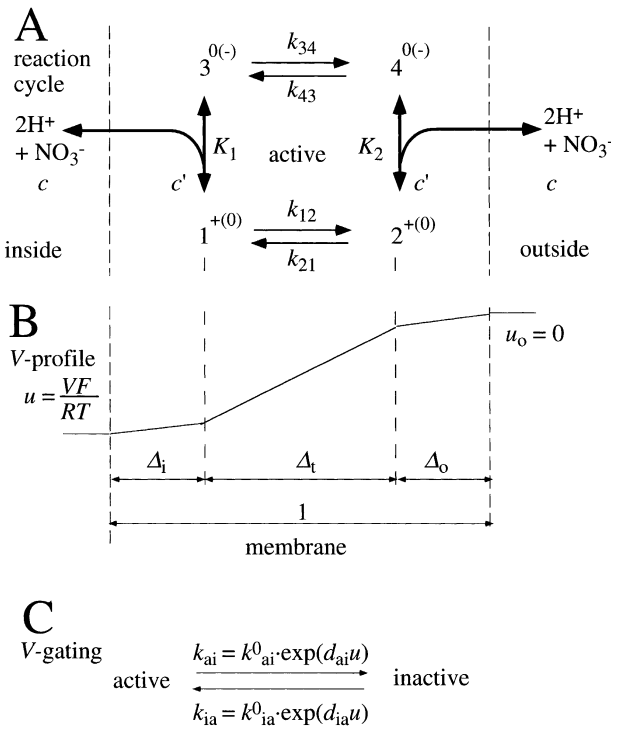

Fig. 1. Definitions of model parameters used. (*A*) Enzymatic reaction cycle for symport of NO_3^- with $2H^+$, where the concentrations c' at the binding sites may differ from the concentrations c in the bulk solutions; binding and debinding reactions are assumed to be fast compared to translocation steps; superscripts on numbered states mark charge number for model versions 1 and 2. (*B*) Hypothetical voltage profile through the membrane, where the transporter experiences only a fraction $\Delta_t < 1$ of the entire voltage, V, and the remaining portion $(1 - \Delta_t)$ is ascribed to an inner and an outer portion Δ_i and Δ_o, respectively. (*C*) Definitions for formal treatment of a simple mechanism for voltage-dependent changes of the activity of an enzyme (V-gating).

ries of reaction steps with correspondingly weaker V-sensitivity, such as a series of binding sites in a pore. Similarly but more specific, Fig. 1*B* illustrates the assumption that V, as measured between the two bulk phases, affects the transport cycle only by a portion Δ_t ($0 < \Delta_t < 1$), whereas Δ_o and Δ_i ($\Delta_t + \Delta_o + \Delta_i = 1$) are external and internal V portions, respectively, that affect the difference between the concentrations c of an ion with the charge z in the bulk and c' immediately at the binding site of the translocating reaction cycle:

$$c'_o = c_o \exp(-z\Delta_o u) \quad \text{and} \tag{1a}$$

$$c'_i = c_i \exp(+z\Delta_i u), \tag{1b}$$

where $u = FV/(RT)$ is the reduced membrane voltage with R, F, and T having their usual thermodynamic meanings. The electrical distances Δ_o and Δ_i may reflect spatial differences through a conducting pore between the membrane surface and the enzymatic binding sites (Gradmann et al. 1997), or the effect of surface charges (Kinraide 2001). In fact, simplification of the model by assuming Δ_o, $\Delta_i = 0$ and $\Delta_t = 1$ (five instead of seven free parameters) yielded inferior fits (*not shown*).

As for the V-dependence of the reaction cycle, two theoretical model versions can be discriminated: In model version 1, the empty enzyme (states 3 and 4) is electroneutral and the charge number $z = +1$ (two H^+ and one NO_3^-) is assigned to the loaded enzyme (states 1 and 2). In model version 2, the empty states 3 and 4 are assumed to be charged with $z = -1$, and the loaded states, 1 and 2, to be neutral. In model version 1, V-dependence is introduced by

$$k_{12} = k^0_{12} \exp(+\Delta_t u/2), \tag{2a}$$

$$k_{21} = k^0_{21} \exp(-\Delta_t u/2), \tag{2b}$$

where the factor 1/2 marks the assumption of a symmetrical Eyring barrier. In model version 2, V-dependence of the reaction cycle is given by

$$k_{34} = k^0_{34} \exp(+\Delta_t u/2), \tag{2c}$$

$$k_{43} = k^0_{43} \exp(-\Delta_t u/2), \tag{2d}$$

and V-independent k_{12} and k_{21}. The four steady-state occupancies,

$$p_1 + p_2 + p_3 + p_4 = 1, \tag{3}$$

can be determined from the four differential equations

$$dp_1/dt = -(k_{12} + k_{13})p_1 + k_{21}p_2 + k_{31}p_3 \tag{4a}$$

$$dp_2/dt = -(k_{21} + k_{24})p_2 + k_{12}p_1 + k_{42}p_4 \tag{4b}$$

$$dp_3/dt = -(k_{32} + k_{34})p_3 + k_{13}p_1 + k_{43}p_4 \tag{4c}$$

$$dp_4/dt = -(k_{43} + k_{42})p_4 + k_{24}p_2 + k_{34}p_3 \tag{4d}$$

With the above assumption (k_{12}, k_{21}, k_{34}, k_{43}, $\ll k_{24}$, k_{41}, k_{13}, k_{31}) and the stability constants, $K_1 = k_{31}/k_{13}$ and $K_2 = k_{42}/k_{24}$, these equations yield

$$p_1 = (k_{21}K_1K_2 + k_{34}K_1)/den \tag{5a}$$

$$p_2 = (k_{12}K_1K_2 + k_{43}K_2)/den \tag{5b}$$

$$p_3 = (k_{21}K_2 + k_{34})/den \tag{5c}$$

$$p_4 = (k_{12}K_1 + k_{43})/den \tag{5d}$$

with $den = k_{12}K_1(K_2 + 1) + k_{21}K_2(K_1 + 1) + k_{34}(K_1 + 1) + k_{43}(K_2 + 1)$. (5e)

The current through the active reaction cycle corresponds to the net translocation rate in counterclockwise direction

$$I_a = p_1k_{12} - p_2k_{21}, \tag{6}$$

for both model versions 1 and 2. In principle, when the rate constants k have their usual dimension of s^{-1}, the right-hand side of Eq. 6 has to be multiplied with the elementary charge, 1.6×10^{-19} As, a charge number and a stoichiometric coefficient to yield the current through an individual, active transporter molecule. Since we do not know whether the recorded steady-state currents are due to a few transporter molecules with large k values or many transporters with small turnover, we simply leave Eq. 6 in its simple form and understand that the k values have the dimension of nA, as the recorded currents do.

Preference of the orientation of the binding site towards the external compartment compared to inside can be expressed for reference conditions by an asymmetry ratio

$$r_{asy} = k^0_{12}k^0_{34}/(k^0_{21}k^0_{43}). \tag{7}$$

We analyzed the apparent steady-state data of $[NO_3^-]_o$-induced current-difference/voltage relationship, *dIV*, data from Zhou et al. (2000) according to Maathuis et al. (1997).

Our additional data comprise not only an extension of the positive voltage range from −30 mV (in Zhou et al. 2000) to +50 mV but also the dynamic behavior of the system. For recordings of complete current-voltage-time relationships, we employed a triangular voltage protocol (Gradmann & Boyd 1999) for voltage-clamp

experiments, which enables one to record actual current-voltage-time relationships within a few seconds. Such recordings allow a detailed analysis of voltage-gating kinetics of transporters with non-linear *I-V* relationships (Gradmann & Boyd 2000). For the present purpose, a simple gating scheme is used for the symporter with an active state (*a*) and an inactive one (*i*). The *V*-sensitive transition probabilities for the transitions from the inactive state to the active one and back are

$$k_{ia} = k_{ia}^0 \cdot \exp(d_{ia}u) \tag{8a}$$

$$k_{ai} = k_{ai}^0 \cdot \exp(d_{ai}u) \tag{8b}$$

where k^0 mark k at $V = 0$ again, and d_{ia}, d_{ai} are the voltage-sensitivity coefficients for k_{ia} and k_{ai}, respectively. The relative activity of the symporter is

$$p_a = 1/(1 + k_{ai}/k_{ia}) \tag{9}$$

and upon a change in voltage from V_0 to V_1, p_a relaxes with the gating time constant

$$\tau_g = 1/(k_{ia} + k_{ai}) \tag{10}$$

with k_{ia} and k_{ai} at V_1. For our purpose, τ_g has not been used explicitly. Here, the temporal changes in p_a have been calculated iteratively for small time increments Δt using the differential equation

$$dp_a/dt = -k_{ai} \cdot p_a + k_{ia} \cdot (1 - p_a). \tag{11}$$

Explicitly, p_a was calculated first by Eq. 9 for steady-state conditions at the holding voltage; and for changing voltages, 1 mV steps per time increment $dt = 10$ ms (as in the command voltage) were used to calculate the actual activity $p_{a,act} = p_{a,prev} + dp_a$ iteratively with the previous activity $p_{a,prev}$ and the changes $dp_a = (-k_{ai} \cdot p_a + k_{ia} \cdot (1 - p_a)) \cdot dt$, using rearranged Equation 11 with the k-values at the actual voltage.

The recorded current

$$I = I_a \cdot p_a \tag{12}$$

is the product of the current I_a through the active reaction cycle (Eq. 6) and the relative activity of the enzyme, i.e. the portion p_a of active molecules.

For the sake of convenience, external NO_3^- is simply considered here as the substrate S and internal NO_3^-, as the product P of the enzymatic process. More precisely, the concentration of the substrate, [*S*], is not simply $[NO_3^-]_o$ but $[NO_3^-]_o \cdot [H^+]_o^2$, and the concentration of the product, [*P*], is $[NO_3^-]_i \cdot [H^+]_i^2$. So, changes in $[NO_3^-]_i$ given here will be overestimates due to imperfect H^+ buffering. We have assumed a constant pH_i of 7.4 according to Zhou et al. (2000). Furthermore, the apparent [*P*] in our calculations does certainly not reflect a uniform distribution within the whole volume of the oocyte. We rather assume [*P*] is a local entity next to the plasma membrane.

The model was fitted to experimental data by using pairs of *dIVt* records taken before ($[NO_3^-]_{i,b}$) and during ($[NO_3^-]_{i,d}$) exposure to external NO_3^-. Ordinary fits could converge to the unrealistic configuration $[NO_3^-]_{i,d} < [NO_3^-]_{i,b}$. Therefore the restriction $[NO_3^-]_{i,d} > [NO_3^-]_{i,b}$ has been implemented in the fitting routine. In some cases absolute $[NO_3^-]_i$ data are presented; in other cases accumulations

$$\Delta[NO_3^-]_i = [NO_3^-]_{i,d} - [NO_3^-]_{i,b} \tag{13}$$

have been calculated for elimination of the history of $[NO_3^-]_{i,b}$. For comparison of two *dIVt* records from conditions *a* and *b*, an accumulation ratio

$$r_{acc} = \Delta[NO_3^-]_{i,a}/\Delta[NO_3^-]_{i,b} \tag{14}$$

has been used for presentation.

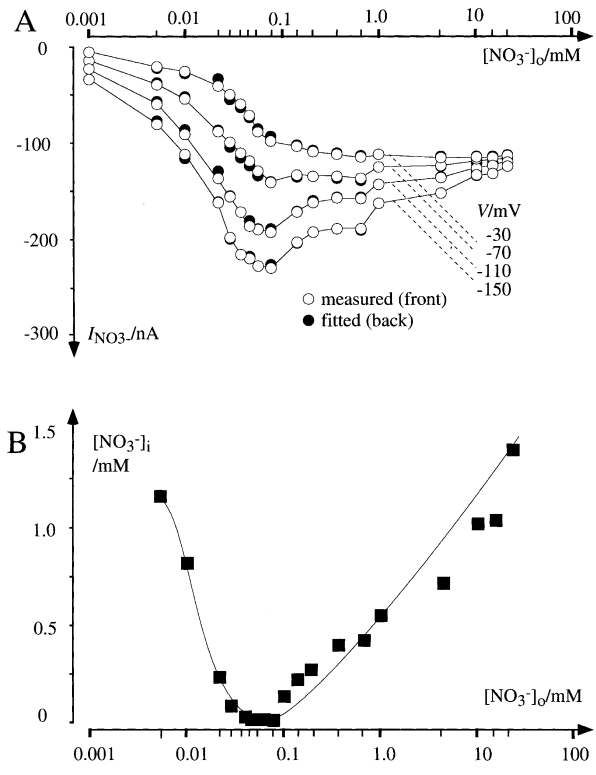

Fig. 2. Fit of model Fig. 1*A*, *B* to experimental data from Fig. 4 in Zhou et al. (2000). (*A*) *Empty circles*: current changes at −30, −70, −110 and −150 mV upon exposures to increasing $[NO_3^-]_o$ compared to control currents at $[NO_3^-]_o = 0$, pH 7. *Filled circles* (partly or totally hidden behind symbols for measured points in cases of part or total coincidence): fitted, $[NO_3^-]_o$-induced currents for all 72 data points (without data from 1 μM $[NO_3^-]_o$ fitted parameters: one $[NO_3^-]_i$ value for each of the applied $[NO_3^-]_o$, and seven common parameters as listed in Table 1 fit# 3. (*B*) Fitted $[NO_3^-]_i$ values; main result: loss of internal NO_3^- at low $[NO_3^-]_o$, and gain at high $[NO_3^-]_o$.

Pairs of *dIVt* records were fit to the model by using a least squares routine, as described by Gradmann et al. (1997). Fitting the model to a pair of *dIVt* records required up to 5 hours calculation time on a 1.2 GHz PC.

For calculations of the temporal changes of $[NO_3^-]_i$ we started with the differential equation

$$d[NO_3^-]_i/dt = k_+ \cdot [NO_3^-]_o - k_- \cdot [NO_3^-]_i, \tag{15}$$

where k_+ is the global rate constant for NO_3^- uptake through the symporter, and k_- the sum of the rate constants for all $[H^+]_i^2 \cdot [NO_3^-]_i$ decreasing processes, such as diffusion from the membrane vicinity to the bulk interior, NO_3^- metabolism, release through the symporter back into the external space, and H^+ buffering. From Eq. 15 we can derive $[NO_3^-]_i(t)$, upon a) addition and b) withdrawal of external $[NO_3^-]$

$$[NO_3^-]_i(t) = ([NO_3^-]_{i,0} - [NO_3^-]_o \cdot k_+/k_-) \times (1 - \exp(-(k_+ + k_-)t) \quad \text{and} \tag{16a}$$

$$[NO_3^-]_i(t) = [NO_3^-]_{i,0} \cdot \exp(-k_- t), \tag{16b}$$

where $[NO_3^-]_{i,0}$ is $[NO_3^-]_i$, at the time of stepwise addition (*a*) or withdrawal (b) of external NO_3^-. For long incubations in external NO_3^-, $[NO_3^-]_i$ approaches the steady-state value $[NO_3^-]_o \cdot k_+/k_-$.

Table 1. Comparison of various fits to the experimental data (open circles in Fig. 2)

#	MV	Reaction cycle						*V* Profile		
		k_{12}^0 nA	k_{21}^0 nA	k_{34}^0 nA	k_{43}^0 nA	r_{asy}	K_1 10^6 mM^{-3}	Δ_i 10^{-3}	Δ_o 10^{-3}	Error nA
1	1	157	138	346	390	1.01	197	20	430	4.04
2	1	198	147	372	288	1.74	201	80	400	3.69
3	**2**	**235**	**435**	**147**	**224**	**0.35**	**98**	**10**	**574**	**3.46**
4	2	218	447	142	242	0.29	98	2	581	3.48

Four-state model as in Fig. 1 with seven free parameters in common; start parameters for odd (even) fit numbers: $k_{12}^0,k_{21}^0,k_{34}^0,k_{43}^0 = 300$ (100) nA; $K_1 = 300\ (100) \cdot 10^6$ mM^{-3}; $\Delta_i, \Delta_o = 0.2$. Model version (MV) 1: states 1 and 2 with $z = 1$, states 3 and 4 with $z = 0$; Model version 2: states 1 and 2 with $z = 0$, states 3 and 4 with $z = -1$; asymmetry ratio r_{asy} (Eq. 7); *bold*, results of #3 illustrated in Figs. 2 and 3.

All calculations have been carried out with a PC using custom-tailored programs written in Turbo Pascal. The software is available on request.

Results

Reanalysis of Previous Steady-State *dIV* Data

The data of $[NO_3^-]_o$-induced currents in Fig. 2 (from Fig. 4 in Zhou et al. 2000) consist of a sequence of nineteen current-voltage relationships, *IV*, each with four measuring points at −30, −70, −110, and −150 mV respectively. In this series of experiments, increasing $[NO_3^-]_o$ were applied, separated by periods of $[NO_3^-]_o = 0$. For each NO_3^- exposure and the preceding control, a *dIV* relationship was recorded. Zhou et al. (2000) did not show data about the temporal behavior of the NO_3^--induced currents, $I_{NO_3^-}$. Consequently, they presented their results as quasi steady-state data. So temporal changes of the transporter activity, e.g., due to *V*-gating, have not been considered by Zhou et al. (2000) nor by our reanalysis of their data (Table 1).

In contrast to Zhou et al. (2000) we assume significant changes of $[NO_3^-]_i$ during the entire series of recordings. Our analysis of their *dIV* curves for various $[NO_3^-]_o$ comprises one $[NO_3^-]_i$ for each *dIV* and seven model parameters (*see* Table 1) that are common for all these *dIV* curves. The *dIV* data for 1 μM $[NO_3^-]_i$ of Zhou et al. (2000) are excluded from our analysis because they spoil the fits to all *dIV* curves.

The agreement of our fitted points with their values in Fig. 2*A* demonstrates that the model of Fig. 1 describes the experimental data quite well. The result that $[NO_3^-]_i$ falls at low $[NO_3^-]_o$ and rises at high $[NO_3^-]_o$ (Fig. 2*B*) confirms our initial conjecture. We regard the initial decline of $[NO_3^-]_i$ as a result of efflux of NO_3^- at low external concentrations.

Theoretically, two model versions should be discriminated: (i) Model version 1: the unloaded binding site (states 3 and 4) is electroneutral, and the loaded binding site (states 1 and 2) carry the charge $z = +1$ ($2\ H^+ + 1\ NO_3^-$), or (ii) Model version 2: the unloaded binding site carries the charge $z = -1$, and the loaded site is electroneutral. More complicated possibilities, e.g., that the loaded form has $z = +2$ and the unloaded $z = +1$, or of apparent non-integer values, are not discussed here.

The error values in Table 1 indicate a preference for model version 2. This preference is also expressed by the stability of the fitted numerical values with respect to the start values: The *k* values differ by only 6 ± 3% between fits 3 and 4, whilst for model version 1 these values vary by 18 ± 15%. The asymmetry ratios are not dramatic. However the $\Delta_i \ll \Delta_o$ seems to be consistent in these results.

The preferred orientation of the binding site towards outside or inside can be given by the asymmetry ratio r_{asy} in Eq. 7, which expresses the orientation of the binding site at reference conditions: $r_{asy} > 1$: towards outside and $r_{asy} < 1$ towards inside. The better fits with model version 2 show an asymmetry towards inside (Table 1).

Figure 3 illustrates the result of the *dIV* analysis from the best fit (#3) in Table 1 for three selected (out of the eighteen) experiments over the range from 10 μM to 20 mM $[NO_3^-]_o$ in an extended *V* range. If $[NO_3^-]_i$ had been constant, the dotted curves for $[NO_3^-]_o = 0$ should coincide, and no intersections should occur, neither amongst the inferred *IV* curves (normal) nor amongst the fitted *dIV* curves (*bold*). This feature holds in Fig. 3 for $[NO_3^-]_o$ 150 μM. For larger $[NO_3^-]_o$, transinhibition of the inward currents by an increase of [*P*] must be considered, i.e., a substantial increase of p_1 by high $[NO_3^-]_i$ will lower $p_2 + p_3 + p_4$ and thus the availability of empty binding sites, p_4, for association of external substrate.

The inferred *IV* curves in Fig. 3 (normal lines) illustrate that at low voltages (e.g. between 0 and −70 mV) the positive currents through the symporter at 10 μM $[NO_3^-]_o$ indicate loss of NO_3^-, and the negative currents for $[NO_3^-]_o$ of 100 μM mark uptake of NO_3^-.

Analysis of New *dIVt* Records with Extended Model

Figure 4*A* shows examples of current records upon exposing a single *Xenopus* oocyte with NrtA to various

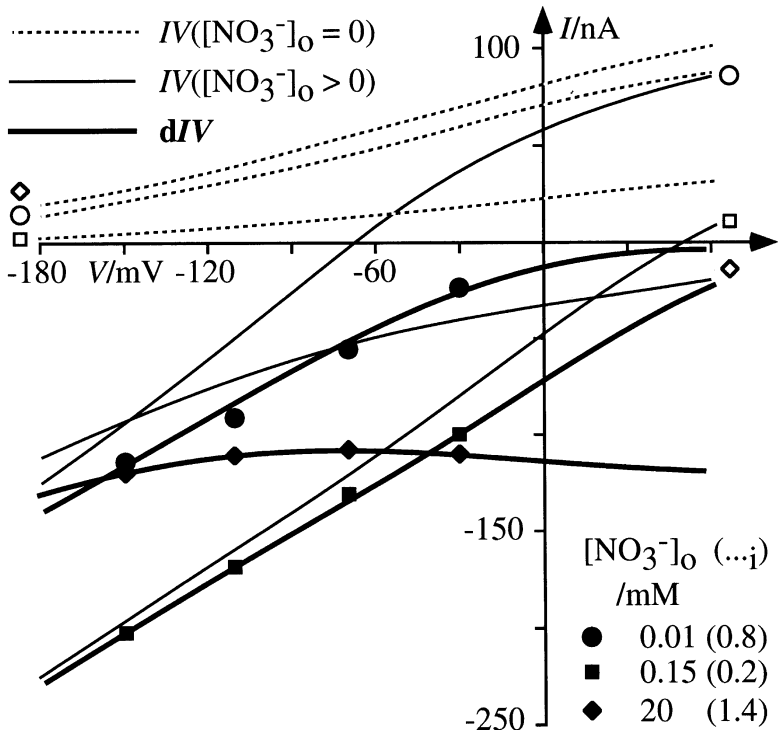

Fig. 3. Three examples out of the eighteen simultaneous fits of the model in Fig. 1*A*, *B* with kinetic parameters as listed in Table 1, #3. *V* range extended compared to measured range. *Bold lines*: fits of difference-currents to data (marked points); *normal lines*: inferred *IV* relationships for the symporter at marked internal and external substrate concentrations; *dotted lines*: inferred *IV* relationships for the symporter at marked internal substrate concentrations and zero $[NO_3^-]_o$; $I_{bold} = I_{normal} - I_{dotted}$.

concentrations of external NO_3^-. In order to eliminate possible drifts, the order of different $[NO_3^-]_o$ was not monotonic but random. This figure shows that increasing $[NO_3^-]_o$ causes increasing amplitudes as well as faster decline after the peak towards a lower steady-state current. Series of this kind have been recorded from several oocytes. The mean peak values (± SEM) of an experiment with $n = 3$ in such a series are displayed in Fig. 4*B* in normal coordinates and in Fig. 4*C* as Lineweaver-Burk plot, which follows normal Michaelis-Menten kinetics with a $K_{1/2}$ of about 13 μM $[NO_3^-]_o$. $K_{1/2}$ (NO_3^-) from four different oocytes varied between 8 μM and 30 μM, and I_{max} between 20 nA and 100 nA at $pH_o = 6.5$ and −40 mV holding voltage, depending on the expression of NrtA and on the pretreatment of the cell with NO_3^- (*see* below). This $K_{1/2} \approx$ 20 μM of our results agrees well with $K_{1/2} \approx 25$ μM of Blatt et al. (1997) and $K_{1/2} \approx 23$ μM in Zhou et al. (2000).

For records of current-voltage-time relationships of the oocyte membrane we performed *V*-clamp experiments with triangular *V* protocol (Fig. 5*A*), typically with a holding voltage, V_0, of −40 mV, a minimum voltage, V_1, of −150 mV and a maximum voltage, V_2, of +50 mV. *V* changes took place in steps of ±1 mV and durations of 10 ms. Figure 5*B* shows examples of the current response in absence (*control*) and presence of 300 μM external NO_3^-. The discontinuities in the current responses at sudden changes of the slope dV/dt are due to the membrane capacitance of the oocyte.

Figure 6*A* shows the same data in *IV* coordinates. It has been pointed out by Gradmann and Boyd (1999) that the crossing points of the 8-shaped, capacity-corrected, *dIVt* records indicate the equilibrium voltage of a predominant and *V*-sensitive ion transporter. However, the records in Fig. 6*A* are not corrected for the membrane capacitance. After this correction, the obvious crossing points of the *dIVt* records would be shifted to more positive voltages, i.e., to about −30 mV, which probably corresponds to the equilibrium voltage, E_{Cl}, of Cl^- electrodiffusion in *Xenopus* oocytes (Miledi & Woodward 1989).

The electrical properties of the $[NO_3^-]_o$-induced event can be examined as the difference between the two *IVt* records in Fig. 6*A*. The subtraction process that yields the *dIVt* curve (Fig. 6*B*) removes details common to both original curves that are not relevant to this study, such as the capacitative effects and crossings within the two parent *IVt* curves, and presents us with the information of interest concerning the response of the nitrate transporter to exposure to external nitrate.

An essential feature of *dIVt* curves is the vertical width of the current loop, i.e., the current differences between rising and falling voltage. These differences mean that this major ion transporter (here NrtA) has a *V*-sensitive activity, $p_a(V, t)$, which relaxes upon *V* changes in the same temporal range as the applied *V* protocol. Only in case of degenerated *IVt* relationships would the currents from ascending and descending *V* coincide, i.e., if the relaxation time constants are much shorter or much longer than the experimental procedure. Such temporal changes of *V*-sensitive ion transporters–known as *V*-gating–are commonly investigated in ion channels using *V*-pro-

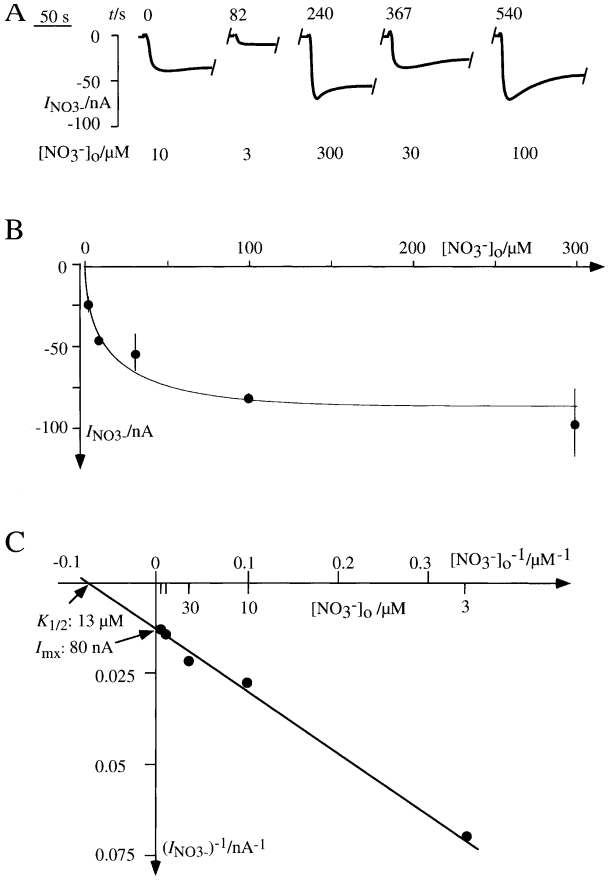

Fig. 4. Current response of *Xenopus* oocytes with NrtA upon exposure to external NO_3^-. (*A*) Individual responses to various $[NO_3^-]_o$ (numbers below traces) at −40 mV holding voltage and pH_o = 6.5. 1 to 3 gaps (4 s) in individual original traces during *IVt* recordings are closed here by interpolation. Numbers above traces: time after start of series of experiments; note: (i) randomized sequence to eliminate possible drift, and (ii) faster relaxation after peak with increasing $[NO_3^-]_o$. (*B*) Titration curve for $[NO_3^-]_o$-induced peak currents: means ± SD (n = 3 for each point); results from a series of experiments on one cell. (*C*) Lineweaver-Burk plot of mean values from panel *B*, yielding an I_{max} of −80 nA and a $K_{1/2}$ of 13 μM NO_3^-.

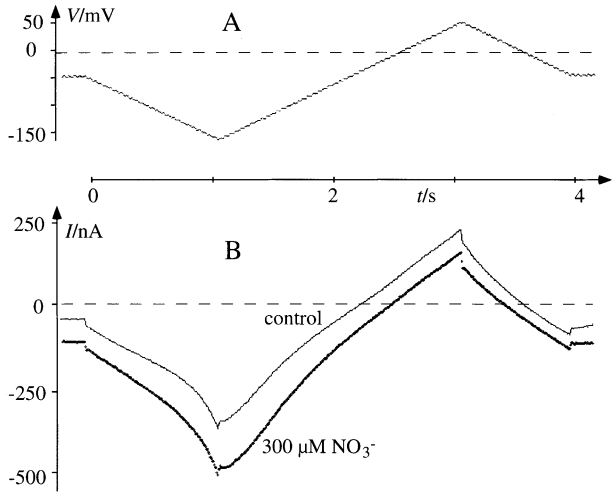

Fig. 5. Triangular voltage protocol (*A*) and current responses (*B*) for current-voltage-time recordings of *Xenopus* oocyte with NrtA; with (300 μM) and without (control) external NO_3^-; pH_o = 6.5; recording close to current peak (*see* Fig. 4); discontinuities in *I* records at kinks in time course of *V* are due to membrane capacitance.

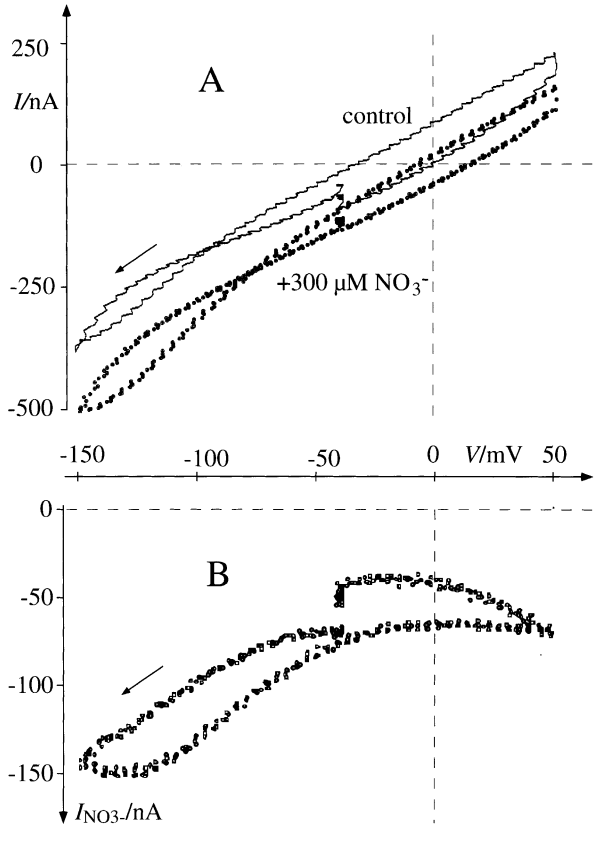

Fig. 6. Results of Fig. 5 plotted in current/voltage diagram. (*A*) Individual tracings with (*points*) and without (*line*) external NO_3^-; arrow indicates direction of measurements. (*B*) Current differences from *A*: *dIVt* record of NO_3^--induced currents.

tocols with large *V*-steps, from which instantaneous currents, steady-state currents, and temporal relaxations can be identified separately.

Our *dIVt* records from triangular *V*-protocols can be acquired more quickly than with step protocols, which is a benefit in case of drifting background conductances. These records basically constitute the complete current-voltage-time relationship of a transporter such as the $2H^+$-NO_3^- symporter NrtA from *E. nidulans*.

A complete analysis of *dIVt* records can be carried out by fitting a detailed model to the data. Some qualitative features, however, can be immediately recognized from inspection of the *dIVt* records. For instance, *dIVt* records, obtained by comparison of two *IVt* records in response to a change in substrate concentration, Δ[*S*], on one side of the membrane ($[NO_3^-]_o$ in our

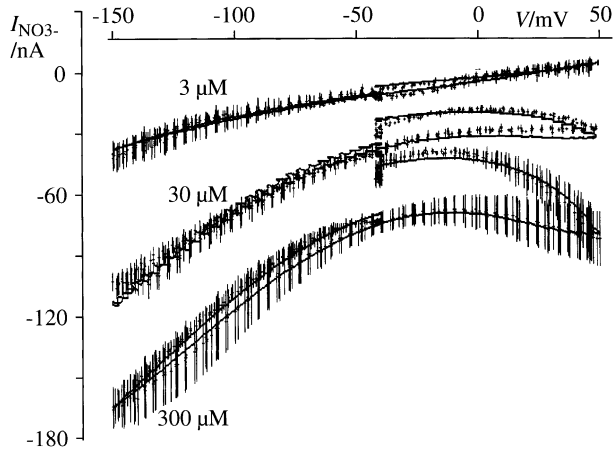

Fig. 7. Effect of $[NO_3^-]_o$ on NO_3^--induced *dIVt* records from *Xenopus* oocytes with NrtA at $pH_o = 6.5$. Three sets of experimental data for different $[NO_3^-]_o$ with $n = 6$ experiments for each set: means (*points*) and ± SEM (*vertical bars*); curves fitted by the model in Fig. 1 with parameters listed in Table 2*A* fit #1.

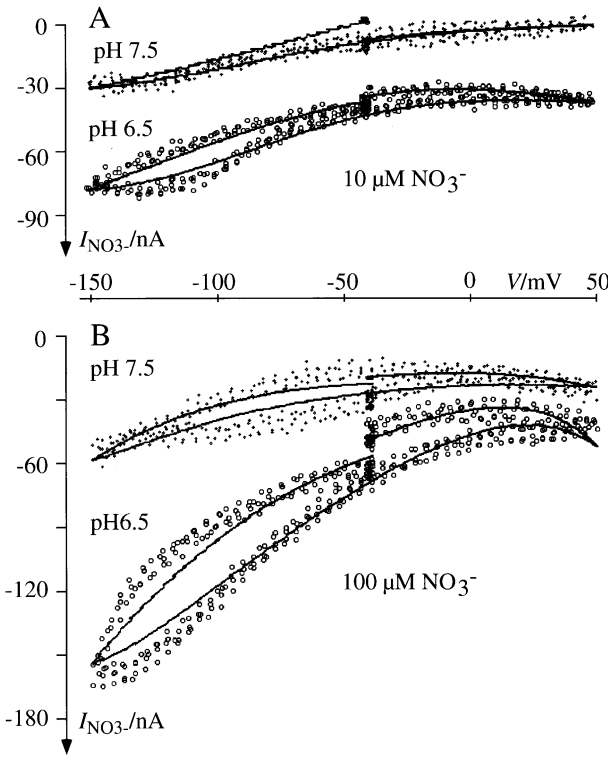

Fig. 8. Effect of pH_o on NO_3^--induced *dIVt* records from *Xenopus* oocytes with NrtA. Induction by exposure to 10 (*A*) and 100 (*B*) μM external NO_3^-. Points: experimental data; curves fitted by the model in Fig. 1 with parameters listed in Table 2*B* fit #3 (*A*), and Table 2*C* fit #1 (*B*).

case), should not intersect with the *V* axis; i.e., the sign of the Δ[*S*]-induced current change should be the same at any *V*. This is the case in the example of Fig. 6*B*.

In the *dIVt* record of Fig. 6*B*, one can assess a conductance increase at negative voltages because the current is still rising after the sign change of the voltage slope at −150 mV. Correspondingly, a conductance decrease at positive voltages can be identified in Fig. 6*B*. Quantitatively, the dynamic characteristics of this phenomenon can be described by the gating factor p_a in Eq. 12, which comprises temporal relationships (Eq. 10) as well.

Figure 7 shows the effect of $[NO_3^-]_o$ on the *dIVt* records at pH_o 6.5. The results of this titration experiment are well fitted by the complete model in Fig. 1 (Eq. 12) with the parameters listed in Table 2*A*. Qualitatively, we notice that the current amplitudes rise less than proportionally with $[NO_3^-]_o$, and that the width of the loop is significantly wider in the more positive voltage range than in the more negative one. Furthermore, the scatter of the experimental data shows a consistent minimum around −30 mV, which means that the scatter is mainly due to fluctuations of the background Cl^- currents, which vanish at E_{Cl} around −30 mV (Miledi & Woodward 1989).

Figure 8 shows that the response of oocytes to changes of external pH, as presented in the *dIVt* records following exposure to 10 μM NO_3^- (*A*) and 100 μM NO_3^- (*B*), is well described by the fits of the model with the parameters listed in Table 2*B*#3 and 2*C*#3. Corresponding to the saturation kinetics of the effect of the concentration of the main substrate NO_3^- in Fig. 7, the model also accounts for the apparent saturation kinetics of the cosubstrate H^+, as found in Fig. 8 where the currents rise less than proportionally with $[H^+]_o^2$.

In order to examine the assumption that $[NO_3^-]_i$ changed significantly during changes in $[NO_3^-]_o$, two kinds of experiments were performed: (i) Analysis of *dIVt* records before incubation and at different times during incubation, which yield fitted $[NO_3^-]_i$ values for each *dIVt* (Fig. 9 and Table 2*D*), and (ii) continuous current recordings at a constant holding voltage during alternating periods of absence and presence of 100 μM external NO_3^-, when decreases and increases of $[NO_3^-]_i$ can be expected, respectively (Fig. 10 and Table 3).

Figure 9 shows a simultaneous fit of the model to two *dIVt* records recorded about 10 and 45 s after the beginning of incubation with 100 μM external NO_3^-. One common reference *IVt* record immediately before incubation has been subtracted from the two *IVt* records. The numerical results of the fits are listed in Table 2*D*. Here, the resulting data for $r_{acc} \approx 4$ are physically realistic with respect to a 4.5 fold incubation time.

Clamp-currents During Periods with and without External NO_3^-

According to our hypothesis of substantial changes in $[NO_3^-]_i$, the decrease of $I_{NO_3^-}$ that follows a peak, upon addition of external NO_3^- (Fig. 4*A*), reflects increasing transinhibition of $I_{NO_3^-}$ by increasing $[NO_3^-]_i$.

Table 2. Fits of model in Fig. 1 to *dIVt* records

#	MV	Active reaction cycle						*V* Profile		*V* Gating				$[NO_3^-]_i$		Error
		k^0_{12} nA	k^0_{21} nA	k^0_{34} nA	k^0_{43} nA	r_{asy}	K_1 10^6 mM^{-3}	Δ_i 10^{-3}	Δ_o 10^{-3}	k^0_{ia} 10^{-3} s^{-1}	d_{ia} 10^{-3}	k^0_{ai} 10^{-3} s^{-1}	d_{ai} 10^{-3}	r_{acc}		nA
A, Fig. 7:														*a*	*b*	
1	**1**	**90**	**186**	**301**	**2417**	**0.06**	**381**	**440**	**5**	**131**	**1130**	**100**	**−475**	**16**	**82**	**3.47**
2	1	134	313	435	19375	0.01	364	470	16	181	930	64	−209	18	102	3.49
3	2	1085	4065	63	485	0.03	24	626	15	729	29	576	−751	6	12	4.98
4	2	10590	834	183	667	3.48	6.8	349	68	186	891	26	−36	98	71	3.49
B, Fig. 8*A*:														*c*		
1	1	906	195	243	353	3.20	945	568	432	226	43	265	−297	9.9		3.36
2	1	1005	1427	178	2598	0.05	430	422	363	250	48	187	−209	10.1		3.43
3	**2**	**248**	**134**	**236**	**1884**	**0.23**	**2754**	**360**	**75**	**369**	**13**	**378**	**−226**	**9.0**		**3.20**
4	2	3876	445	795	917	7.55	541	552	448	558	27	167	−104	9.9		3.37
C, Fig. 8*B*:														*c*		
1	**1**	**3162**	**119**	**6718**	**5736**	**22.7**	**107**	**493**	**226**	**1028**	**7**	**551**	**−216**	**10.3**		**7.83**
2	1	1966	110	3339	6382	34.2	97	483	243	649	17	463	−242	10.3		7.99
3	2	6870	371	1591	1167	13.6	113	203	192	1577	20	616	−180	10.4		7.88
4	2	9761	536	1313	3824	53.0	37	357	146	2352	15	516	−157	10.2		7.86
D, Fig. 9:														*d*		
1	1	3242	58	543	448	67.7	1477	198	341	256	743	252	−435	4.4		4.938
2	1	645	175	1867	1013	6.79	3873	323	160	274	725	39	−5	4.8		4.95
3	**2**	**3559**	**361**	**59**	**1103**	**0.53**	**602**	**337**	**109**	**234**	**793**	**211**	**−456**	**3.9**		**4.936**
4	2	2131	213	1688	96	176	1008	172	167	244	758	218	−497	4.4		5.09

Start parameters for odd (even) #: k^0_{12}, k^0_{21}, k^0_{34}, k^0_{43} = 300 (1000) nA; K_1 = 300 (100) · 10^6 mM^{-3}; Δ_i, Δ_o = 0.3 (0.1) or 0; k^0_{ai}, k^0_{ia} = 0.3 (0.1) s^{-1}; d_{ai}, d_{ia} = 0.3 (0.1); $[NO_3^-]_{i,b}$, $[NO_3^-]_{i,d}$ = 100 μM; Model version (MV) 1: states 1, 2 with $z = 1$ and 3, 4 with $z = 0$; MV 2: states 1, 2 with $z = 0$ and 3, 4 with $z = -1$; asymmetry ratio r_{asy}, Eq. 7; accumulation ratio r_{acc}, Eq. 14; *a*: $r_{acc,30\ \mu M/3\ \mu M}$; *b*: $r_{acc,\ 300\ \mu M/3\ \mu M}$; *c*: $r_{acc,\ pH\ 6.5/pH\ 7.5}$; *d*: $r_{acc,\ 45\ s/10\ s}$; **bold:** best fits.

$[NO_3^-]_i(t)$, following alternating periods of presence and absence of external NO_3^- (Fig. 10*A*), is calculated by Eqs. 16a, b and illustrated in Fig. 10*B*, together with the time course of $I_{NO_3^-}$ as the oocyte responds to inhibition by $[NO_3^-]_i$ (Fig. 10*C*; dashed line, theoretical; continuous line, observed as in Fig. 4*A*).

The time course of $[NO_3^-]_i$, following alternating periods of presence and absence of external NO_3^- (Fig. 10*A*), is calculated by Eqs. 16a, b and illustrated in Fig. 10*B*, together with the response of $I_{NO_3^-}$ to inhibition by $[NO_3^-]_i$ (Fig. 10*C*; continuous line, observed as in Fig. 4*A*; dashed lines, theoretical). Several parameters, defined in Fig. 10*C*, allow determination of the time constants $\tau_- = 1/k_-$ and $\tau_+ = 1/(k_+ + k_-)$, using the relationships given by the inset in Fig. 10*C*, where k_+ and k_- are, respectively, the rate constants for the cellular uptake and decrease of nitrate.

$I_{NO_3^-}$ has been recorded over a series of exposures to 100 μM external NO_3^- for various times t_1, with following periods of recovery, t_2, also of variable duration. The individual events have been analyzed systematically according to Fig. 10, and are listed in Table 3. The average $\tau_- \approx 10$ min, corresponding to $k_- = 1/\tau_- \approx 0.0017$ s^{-1}, reflects the decay of a local accumulation of $2H^+ + NO_3^-$ inside near the membrane (*i*) into the bulk volume of the cell, (*ii*) into the N metabolism, and (*iii*) back through the symporter. Clearly, subsummation of all these processes under only one rate constant, k_-, is a coarse approach. With $k_- \approx 0.0017$ s^{-1} and the average $\tau_+ \approx 1$ min (Table 3), we obtain an apparent $k_+ = 1/\tau_+ - k_- \approx 0.015$ s^{-1} for uptake through the symporter at 100 μM external NO_3^-. With the assumption that the apparent k_+ rises and falls proportionally with $[NO_3^-]_o$, the velocity of the exponential decrease of $I_{NO_3^-}$ from the peak I_0 toward I_∞, with the time constant $\tau_+ = 1/(k_+ + k_-)$, should also rise and fall proportionately with $[NO_3^-]_o$. This behavior is confirmed by the results in Fig. 4*A*.

According to our hypothesis of $I_{NO_3^-}$ inhibition by internal NO_3^-, this inhibition should rise with the time t_1 of the preceding exposure and fall with the time t_2 of the succeeding recovery. Therefore the inhibition should rise with t_1/t_2 up to maximum inhibition, which is reached at I_∞. In our series of experiments with exposures to $[NO_3^-]_o$ of 100 μM, I_∞ was 27 ± 8% of I_{max} (Table 3). Based on the data from Table 3, Fig. 11 illustrates these relationships between I_0, t_1/t_2, I_{max}, and I_∞.

The results of the kinetic analysis can be used for further calculations and cross-examinations. For instance, $k_+ \approx 0.015$ s^{-1} at 100 μM external NO_3^-, and $k_- \approx 0.0017$ s^{-1}, yield a steady-state $[NO_3^-]_i = [NO_3^-]_o\, k_+/k_- \approx 1$ mM, which is roughly confirmed by the data in the inset of Fig. 9 ($[NO_3^-]_i \approx 0.5$ mM after 45 s incubation and subject to further increase to-

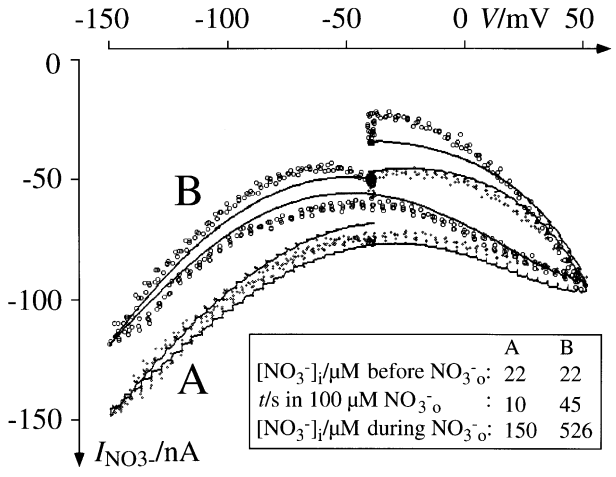

Fig. 9. Inhibiting effect of prolonged exposure to NO_3^- on NO_3^--induced *dIVt* records from *Xenopus* oocytes with NrtA. Description of effect by increasing $[NO_3^-]_i$ (more precisely: $[NO_3^-]_i \cdot [H^+]_i^2$). Points: experimental data; curves fitted by model in Fig. 1 with parameters listed in Table 1*C* fit #3; inset: numerical result of fit for increase of internal substrate.

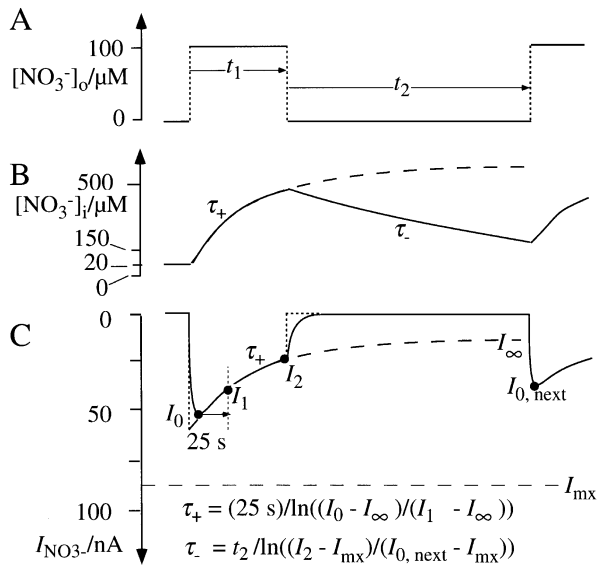

Fig. 10. Definitions of parameters for analysis of series of current records during alternating exposures to 0 and 100 μM external NO_3^-. Numerical data correspond to example in Fig. 4*A* at pH_o = 6.5 and −40 mV holding voltage. (*A*) Protocol of NO_3^- exposure. (*B*). Hypothetical time course of inhibiting $[NO_3^-]_i$ (more precisely: $[NO_3^-]_i \cdot [H^+]_i^2$). (*C*) Schematic time course of current record. Efflux (of NO_3^- + $2H^+$) ignored; dotted lines at I_0 and I_2 mark idealized time course, compared to more realistic wash-in and-out kinetics (*solid curve*); dashed lines mark maximum effect I_{max} (after complete recovery) and extrapolation to steady-state, I_∞.

wards the steady-state level). The apparent steady-state accumulation $[NO_3^-]_i/[NO_3^-]_o = k_+/k_- \approx 10$ is, however, much smaller than the theoretical, thermodynamic equilibrium ratio $[NO_3^-]_i/[NO_3^-]_o = ([H^+]_o/[H^+]_i)^2 \cdot \exp(V_h F/(RT)) \approx 300$ at pH_o = 6.5, pH_i = 7.4, and the holding voltage V_h = −40 mV. This discrepancy may reflect the fact that the theoretical accumulation ratio holds for a thermodynamic equilibrium, whereas the apparent accumulation ratio is a steady-state feature. In this case, the portion of k_- due to NO_3^- outward release through the symporter is only about 3%, and the portion of k_- attributable to N-metabolism and NO_3^- diffusion to the bulk interior is almost 100%.

Discussion

The results presented here strongly support the idea that NrtA-mediated uptake of NO_3^- in *Xenopus* oocytes can easily result in increased concentrations of $[NO_3^-]_i$ that result in transinhibition of NrtA-mediated $I_{NO_3^-}$. This interpretation employs a straightforward enzymatic reaction cycle for $2H^+$-NO_3^- symport and does not require an extra inhibiting site, as has been proposed by Zhou et al. (2000).

The portion of the oocyte volume associated with these $[NO_3^-]_i$ changes must be only a fraction of the whole cell volume, in which $[NO_3^-]_i$ does not seem to change substantially following exposures to external NO_3^-. For a first appraisal of this situation we assume an oocyte volume, V_{oo}, of about 10^{-9} m^3, and an $I_{NO_3^-}$ of 100 nA (e.g., Fig. 2), corresponding to an uptake rate $J = I/F$ of 10^{-12} mol s^{-1} with the Faraday constant $F \approx 10^5$ As mol^{-1}, and a total $[NO_3^-]_i$ increase of $d[NO_3^-]_{i,tot}/dt = J/V_{oo} \approx 10^{-3}$ mol $\cdot$ m^{-3} s^{-1} = 1 μM s^{-1}. The inset in Fig. 9 shows $d[NO_3^-]_i/dt$ 10 μM s^{-1}, indicating that the fitted $[NO_3^-]_i$ values in this study reflect a compartment of about 10% of the total cell volume, at the inner side of the plasma membrane.

In general, the good fits in this investigation seem to validate the model. However, some details deserve to be commented upon. One aim of this study was to possibly discriminate between the two model versions 1 and 2. Table 1 seems to point to a preference of model 2 because it provided the better fits and stable solutions, i.e., solutions that are insensitive to the magnitude of the start parameters. However, this preference could not clearly be confirmed by the corresponding results in Table 2.

A more significant difference between the seven model parameters for the transport process in Table 1 and Table 2 is found in the parameters Δ_i and Δ_o, which characterize the voltage profile: $\Delta_i \ll \Delta_o$, in Table 1 and $\Delta_i \gg \Delta_o$ in Table 2 with similar $\Delta_t \sim 0.5$ in both tables. The results indicate that the apparent differences between Δ_i and Δ_o do not correlate with the model versions 1 and 2, as they might do theoretically. We rather interpret this discrepancy between Tables 1 and 2 the following way:

In the model for the results in Table 1, the nonlinearity of the steady-state *IV* relationships is a feature of the fully active transport system. In contrast, the model for Table 2 comprises the additional gating

Table 3. Series of current events induced by exposure to 100 μM NO_3^- for various durations, t_1, and recovery times, t_2, before next event; experimental data and temporal analysis

Event	I_0/I_{max}[1]	I_1/I_{max}	I_2/I_{max}	I_∞/I_{max}	t_1 s	t_2 s	τ_+ s	τ_- s
1	0.59	0.50	0.41	0.30	72	2400	67	–
2	1.00	0.67	0.32	0.30	220	72	38	234
3	0.50	0.41	0.35	0.32	43	264	35	517
4	0.61	0.50	0.50	0.32	31	330	50	1096
5	0.63	0.52	0.47	0.26	43	60	68	–
6	0.47	0.41	0.31	0.22	20	38	87	371
7	0.41	0.32	0.28	0.26	67	91	26	890
8	0.35	0.30	0.22	0.24	91	163	49	337
9	0.50	0.43	0.28	0.22	94	148	77	514
10	0.46	0.41	0.24	0.30	103	3600	103	–
11	1.00	0.82	0.54	0.30	113	115	81	346
12	0.67	0.59	0.54	0.30	36	120	98	727
13	0.61	0.54	0.39	0.30	100	–	94	–
Mean							67	558
± SD							±27	±287

[1] $I_{max} = -18$ nA in this particular experiment. For definitions, *see* Fig. 10.

factor p_a (in Eq. 12), which has a non-linear steady-state V-sensitivity of its own. Therefore, we conclude that $\Delta_i \gg \Delta_o$ in Table 2 reflects the 'true' voltage profile of the active transport process, and that the apparent $\Delta_i \ll \Delta_o$, in Table 1 is due to disregarding the V-dependent gating factor p_a.

Because the model with gating (Eq. 12) is more realistic, we focus on the results in Table 2 to extract some physical features of the transporter.

1. The shape of the voltage profile with $\Delta_i \sim 0.4$, $\Delta_t \sim 0.5$, $\Delta_o \sim 0.1$, means that the transporter experiences about 50% of the electric field, and that the catalytic process takes place more in the external than in the internal portion of the plasmalemma.

2. From the four best fits (*bold*) three asymmetry ratios are <1. This may indicate that–in the absence of V- and substrate gradients–the binding site of the transporter is preferentially oriented to the internal side of the membrane. However, the statistical support for this observation is poor.

3. As for gating, the apparent gating charge $z_g = d_{ia} - d_{ai}$ is positive for inactivation throughout, and the ratio k^0_{ia}/k^0_{ai} is about 1 with k^0 values of several 100 s^{-1}. This means that the transporter is active at negative and inactive at positive voltages with half activity around $V = 0$, and relaxation times (Eq. 10) of a few ms.

Although V-gating of ion channels is a major subject of electrophysiology, little is known about V-gating of other ion transporters. As for $2H^+$-anion symporters, our results confirm the increasing slope of the IV curve of the of $2H^+$-Cl^- symporter in *Chara* (Beilby & Walker 1981) and for the nitrate transporter in *Neurospora* (Blatt et al. 1997). The inactivation of anion symporters at positive voltages may have the physiological benefit of avoiding loss of anions (here NO_3^-) through the symporter in case of electroosmotic stress, i.e., in situations of small (negative) resting voltage when the generation of electrochemical energy (proton-motive force) no longer satisfies the consumers.

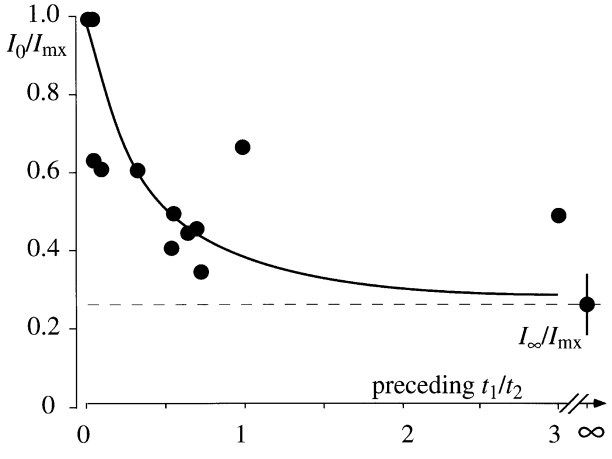

Fig. 11. Effect of preceding exposure times, t_1, and recovery times, t_2, on peaks of relative currents, I_0/I_{max}, upon exposure to 100 μM external NO_3^-; data from Table 3.

The results in Fig. 9, Table 3 and Fig. 11 strongly support the straightforward hypothesis of transinhibition of NO_3^- uptake through NrtA by internal NO_3^-. It is recalled that the complete substrate of NrtA is not NO_3^- only, but $2H^+ + NO_3^-$. This means that the role of $[NO_3^-]$ discussed here applies equally for $[H^+]^2$, i.e., changes of pH_i could not only have the stoichiometric effect discussed above, but internal H^+ might alternatively inhibit NrtA by an allosteric mechanism. A variety of alternative explanations exists that are more complicated than the model presented here, but they are without rigorous experimental support.

As for the mechanism and velocity of the spontaneous decay of local NO_3^- accumulations inside, we

assume diffusion impeded by cytoplasmic obstacles, especially endomembranes. For a crude numerical estimate, we assume diffusion velocities of good electrolytes around 1 μm per ms, corresponding to 0.1 mm in 10 s; so, after occurrence of a local accumulation near the membrane, the bulk concentration in oocytes with 1 mm diameter would still be far from being equilibrated after 10 s. Since diffusion is not free but slowed down by cytoplasmic structures, probably by more than a factor of 10, our results of τ_- in the 100 s range (Table 3) support the simple hypothesis of diffusion-mediated decay of local product accumulations.

In a wider physiological context, one may ask why similar accumulation of substrate has not been reported from other symporters, especially the Na^+/glucose transporter, SGLT (for review *see* Wright et al. 1994), which can mediate currents up to 1 μA when expressed in *Xenopus* oocytes. A reason for this discrepancy may be that glucose is more rapidly metabolized than NO_3^-. Another possibility is that the absolute concentrations $[P] = [H]_i^2[NO_3^-]_i$ of Nrt are very small compared with the $[P]$ of SGLT (Na and glucose), so for a given flux, the relative changes of $[P]$ will be much larger for Nrt compared to SGLT.

This research has been supported by grants from the Natural Sciences and Engineering Research Council of Canada to C.M.B., and is a cooperative effort between Dalhousie University and the Institute of Marine Biotechnology of the National Research Council of Canada. This is NRC publication number 42374.

References

Beilby, M.J., Walker, N.A. 1981. Chloride transport in *Chara*. I. Kinetics and current-voltage curves for a probable proton symport. *J. Exp. Bot.* **32:**43–54

Blatt, M.R., Maurousset, L., Meharg, A.A. 1997. High-affinity $NO_3^-H^+$ cotransport in the fungus *Neurospora*: Induction and control by pH and membrane voltage. *J. Membrane Biol.* **160:**59–76

Glass, A.D.M., Britto, D.T., Kaiser, B.N., Kinghorn, J.R., Kronzucker, H.J., Kumar, A., Okamoto, M., Rawat, S., Siddiqi, M.Y., Unkles, S.E., Vidmar, J.J. 2002. The regulation of nitrate and ammonium transport systems in plants. *J. Exp. Bot.* **53:**855–864

Goldin, A.L. 1992. Maintenance of *Xenopus laevis* and oocyte injection. *Methods in Enzymology* **207:**266–279

Gradmann, D., Boyd, C.M. 1999. Electrophysiology of the marine diatom *Coscinodiscus wailesii* IV: Types of non-linear current-voltage-time relationships recorded with single saw-tooth voltage-clamp. *Europ. Biophys. J.* **28:**591–599

Gradmann, D., Boyd, C.M. 2000. Three types of membrane excitations in the marine diatom *Coscinodiscus wailesii*. *J. Membrane Biol.* **175:**149–160

Gradmann, D., Johannes, E., Hansen, U.P. 1997. Kinetic analysis of Ca^{2+}/K^+ selectivity of an ion channel by single-binding-site models. *J. Membrane Biol.* **159:**169–178

Gradmann, D., Klieber, H.G., Hansen, U.P. 1987. Reaction kinetic parameters for ion transport from steady-state current-voltage curves. *Biophys. J.* **51:**569–585

Kinraide, T. 2001. Ion fluxes considered in terms of membrane-surface electrical potentials. *Austr. J. Plant Physiol.* **28:**605–616

Maathuis, F.J.M., Sanders, D., Gradmann, D. 1997. Kinetics of high affinity K^+ uptake in plants, derived from K^+-induced changes in current-voltage relationships. *Planta* **203:** 229–236

Miledi, R., Woodward, R.M. 1989. Effects of defollication on membrane current responses of *Xenopus* oocytes. *J. Physiol.* **416:**601-621

Stühmer, W. 1992. Electrophysiological recording from *Xenopus* oocytes. *Methods in Enzymology* **207:**319–339

Unkles, S., Hawker, K.L., Grieve, C., Campbell, E.I., Kinghorn, J.R. 1991. crnA encodes a nitrate transporter in *Aspergillus nidulans*. *Proc. Natl. Acad. Sci U.S.A.* **88:**204–208

Wright, E.M., Loo, D.D., Panayotova-Heiermann, M., Lostao, M.P., Hirayama, B.H., Boorer, K., Zampighi, G. 1994. 'Active' sugar transport in eukaryotes. *J. Exp. Biol.* **196:**197–212

Zhou, J.J., Trueman, L.J., Boorer, K.J., Theodoulou, F.L., Forde, B.G., Miller, A.J. 2000. A high affinity fungal nitrate carrier with two transport mechanisms. *J. Biol. Chem.* **275:**39894–39899